ADVANCED MATERIALS

Supporting Information

for *Adv. Mater.*, DOI 10.1002/adma.202301414

From Nanoalloy to Nano-Laminated Interfaces for Highly Stable Alkali-Metal Anodes

Parham Pirayesh, Karnpiwat Tantratian, Maedeh Amirmaleki, Feipeng Yang, Enzhong Jin, Yijia Wang, Lyudmila V. Goncharova, Jinghua Guo, Tobin Filleter, Lei Chen and Yang Zhao**

Supporting Information

From Nanoalloy to Nano-Laminated Interfaces for Highly Stable Alkali-Metal Anodes

Parham Pirayesh[1+], Karnpiwat Tantratian[2+], Maedeh Amirmaleki[3,6+], Feipeng Yang[4], Enzhong Jin[1], Yijia Wang[1], Lyudmila V. Goncharova[5], Jinghua Guo[4], Tobin Filleter[3], Lei Chen[2], Yang Zhao[1*]*

[1]Department of Mechanical and Materials Engineering

University of Western Ontario, London, Ontario, N6A 5B9, Canada

Email: Y. Zhao: yzhao628@uwo.ca

[2]Department of Mechanical Engineering
University of Michigan−Dearborn, Dearborn, Michigan 48128, United States
Email: L. Chen: leichn@umich.edu

[3]Department of Mechanical and Industrial Engineering
The University of Toronto, Toronto M5S 3G8, Canada

[4]Advanced Light Source
Lawrence Berkeley National Laboratory, Berkeley, CA, 94720, United States

[5]Department of Physics and Astronomy

University of Western Ontario, London, ON N6A 3K7, Canada

[6]Department of Materials Science and Engineering,

Massachusetts Institute of Technology, Cambridge, MA 02139, United States

+ These authors contributed equally to this work.

Materials and Methods

Al_2O_3-alucone hybrid coating: A fresh Na foil with a diameter of 3/8 inch was prepared with the aid of a homemade press machine by pressing a piece of sodium metal stick (from Aldrich) as a starting sodium metal. Al_2O_3-alucone hybrid coatings were conducted in a Gemstar-8 ALD system (Arradiance, USA) directly connected with the argon-filed glove box. For the ALD Al_2O_3 process, trimethylaluminium (TMA) and water (H_2O) were used as precursors. For MLD alucone process, TMA and ethylene glycol (EG) were used as precursors, in which EG was heated at 85 ^oC to get vapor. The ALD process used as 0.1 s/30 s/0.1 s/50 s TMA pulse/purge/ H_2O pulse/purge sequence. The MLD process used as 0.1 s/40 s/0.1 s/70 s TMA pulse/purge/EG pulse/purge sequence. Three unit structures were demonstrated: one layer of ALD Al_2O_3 with one layer of MLD alucone, two layers of ALD Al_2O_3 with two layers of MLD alucone, and five layers of ALD Al_2O_3 with five layers of MLD alucone. Three types of unit structures are named: 1ALD-1MLD, 2ALD-2MLD, and 5ALD-5MLD, respectively. In addition, different thicknesses have been further investigated for each unit structure d by applying different ALD/MLD cycles. For example, for the 1ALD-1MLD unit structure, we repeat the deposition for this unit structure with different cycles to obtain the different thicknesses of the nano-laminated layers, including 5 cycles, 10 cycles, and 25 cycles. The samples for 1ALD-1MLD unit structures with different thicknesses are named: (1ALD-1MLD)5, (1ALD-1MLD)10 and (1ALD-1MLD)25, respectively. Similar processes have been applied to the other two types of unit structures for the different thicknesses. In order to demonstrate the unique feature of the rational-designed nano-laminated hybrid interface, both Li and Na metal anodes are used for comparison. The ALD/MLD deposition temperature for Li and Na anodes are 90 ^oC and 120 ^oC, respectively.

Electrochemical measurements: The electrochemical performance was analyzed in CR2032 coin-type cells. The coin cells were assembled in an ultra-pure argon-filled glove box by symmetrical Na(Li)/electrolyte-separator/Na(Li) system using a polypropylene separator (Celgard 3501 for Na system and Celgrad 2400 for Li system). The electrolyte used for Na/Na symmetrical cell is 1 M sodium triflate ($NaSO_3CF_3$ 98%, Sigma-Aldrich) dissolved in diethylene glycol dimethyl ether (reagent grade ≈98%, Sigma-Aldrich, predried before usage). The electrolyte used for Li/Li symmetrical cell is a carbonate-based electrolyte (1 M $LiPF_6$ in EC: DEC: DMC with 5 % FEC). The amount of electrolyte used for all the samples was ~ 30 uL. The stripping/plating studies were carried out on a Land 2001A Battery Test System and Neware Battery Test System

at room temperature. A constant current was applied to the electrodes during repeated stripping/plating while the potential was recorded over time in the symmetric cell testing.

Na-$Na_3V_2(PO_4)_3$ (NVP) batteries were tested via CR2032 cells using protected Na (Na@(1ALD-1MLD)10) with carbonate-based electrolyte (1M $NaPF_6$ in EC/DEC/FEC). The $Na_3V_2(PO_4)_3$ electrodes were prepared by casting a N, N-Dimethylformamide (NMP) slurry containing $Na_3V_2(PO_4)_3$, Super P and poly(vinylidene difluoride) (PVDF) in a weight ratio of 8:1:1 onto carbon-coated Al foil. The cathodes were cut into discs with a diameter of 10 mm and dried at 80 ^oC prior to use. The areal loading of $Na_3V_2(PO_4)_3$ is about 3 mg cm^{-2}. The electrolyte amount used for Na-NVP batteries was ~ 30 uL.

Characterization: For the characterization after cycling, the batteries were first disassembled in the glove box and then gently rinsed with dimethyl carbonate to remove residual Li salts and electrolytes. The electrodes were sealed inside the Ar-filled tubes before characterization. SEM images were taken using a Hitachi 3400N Environmental SEM and Hitachi 4800 at an acceleration voltage of 5 kV.

Rutherford Backscattering Spectroscopy (RBS) spectra were obtained using 2.5 MeV He^{++} ions at the Tandetron accelerator facility at Western University with a Si detector positioned at 170^o in Cornell geometry. Due to the sensitive nature of these samples, Li and Na samples were handled in an Ar-filled dry bag, before they were introduced to the RBS vacuum chamber. An sb-implanted amorphous Si sample with a known Sb content of 4.82 $\times 10^{15}$ atoms /cm^2 was used for calibration. The RBS results were then fitted using the MEIS software to determine the elemental depth profile.

ToF-SIMS measurements were conducted using an ION-TOF (GmbH, Germany) ToF-SIMS IV with a bismuth liquid metal ion source in the Surface Science Western. The base pressure of the analysis chamber was ~10^{-8} mbar. The action of the primary ion beam bombardment on the sample surface induces the emission of negative secondary ions. The analysis area was 400 × 400 μm^2 (or 500 × 500 μm^2). Sputtering with a Cs^+ ion beam (3 keV) was used for depth profiling analysis with the sputtering areas of 200 × 200 μm^2.

Synchrotron Al K-edge X-ray absorption spectroscopy (XAS) measurements were conducted on Beamline 7.3.1 of the Advanced Light Source at Lawrence Berkeley National Laboratory.

Mechanical properties measurements: A TEM grid with a holey SiN_4 window with a hole diameter of 2.5 μm (Ted Pella Inc.) covered by single-layer chemical vapor deposited graphene was used as support for deposited films. AFM deflection tests were conducted using an Asylum MFP-3D

AFM. A cantilever with a diamond tip of ~100 nm tip radius (ND-DYI series, All-Diamond Probe, Nano Science Instrument) was used and calibrated using Sader's method yielding a normal spring constant of 34 Nm^{-1}.

Cohesive Zone Model (CZM): The mechanical analysis of SEI delamination is performed using the Solid Mechanics module in COMSOL Multiphysics. The 2D structure is divided into damaged and undamaged regions, and the adhesion force is modelled using the Cohesive Zone Model (CZM). In this work, we assume that the CZM follows a bilinear traction-separation law in which traction (T) linearly increases with separation (δ) until reaching a maximum value T_{max}, and then T linearly decreases to zero at a critical separation (δ_{max}), as shown in **Figure S27**. The values of the parameters and material properties used in the model are listed in **Table S1**. The left boundary is subjected to a roller constraint and the right boundary is fixed. Pressure is applied to the damaged region to simulate the growth of dendrites. From the theoretical analysis ($\sigma V_m = F\Delta\emptyset$, Equation 1), under the same charging condition, the pressure from Li is approximately 1.82 times larger than that from Na. The range of SEI thickness studied is 4-20 nm, and the stationary solver is used, with mesh convergence analysis performed. The output includes stress and displacement/crack opening of the SEI, and the displacement of the left boundary is measured as a proxy for the size of the dendrite nucleus.

Phase-field Model for Dendrites with SEI Mechanics: This phase-field model is an extension of an original model developed by L. Chen et al. that describes the morphology of electrodeposited materials based on electrochemical driving forces. The new model adds the mechanics of the SEI to the electrochemical model, which enables the examination of how the SEI mechanics and electrodeposition behavior interact with one another. The order parameter (ξ) is used to describe the two distinct phases of the anode (ξ = 1) and the electrolyte (ξ = 0). The moving interface is driven by interfacial energy and the driving force from the electrode reactions. The equation can be thus expressed as,

$$\frac{\partial \xi}{\partial t} = -L_0(g'(\xi) - k\nabla^2\xi) - L_\eta h'(\xi)\left\{\exp\frac{(1-\alpha)F\eta_a}{RT} - c_+\exp\left[\frac{-\alpha F\eta_a - F\eta_m}{RT}\right]\right\}$$

where L_0 and L_η are the coefficients related to the interfacial energy and reaction, respectively. the interpolation function is described as, $h(\xi) = \xi^3(10 - 15\xi + 6\xi^2)$. $\eta_m = CPv_m/F$ is and mechanical, written as a function of hydrostatic pressure, *P* at the anode/SEI interface. Generally, the presence of the mean compressive stress slows down the electrodeposition reaction, while the

tensile stress shows the opposite. The details of this mechanical overpotential term in phase-field model can be found in K. Tantratian et al. The phase-field equation is solved simultaneously with other 3 governing equations: charge conservation, mass transport, and stress equilibrium equations. The diffusion of ionic species can be described as,

$$\frac{\partial c_+}{\partial t} = \nabla \cdot \left[D^{eff} \nabla c_+ + \frac{D^{eff} \nabla c_+}{RT} nF \nabla \phi \right] - \frac{c_s}{c_0} \frac{\partial \xi}{\partial t},$$

where $D^{eff} = h(\xi) D_{metal} + (1 - h(\xi)) D_e$ is the effective diffusion coefficient. D_{metal} and D_e are diffusion coefficients of ionic species in the metal electrode and the electrolytes, respectively. The electrostatic potential is governed by the charge conservation equations, expressed as,

$$\nabla \cdot [\sigma^{eff} \nabla \phi] = I_R,$$

where $\sigma^{eff} = h(\xi)\sigma_{metal} + (1 - h(\xi))\sigma_e$ is the effective conductivity. The source term, $I_R = nFc_+ \partial \xi / \partial t$, is non-zero at the metal/electrolyte interface due to the reaction. Lastly, the stress equilibrium equation is written as,

$$\nabla \cdot \boldsymbol{\sigma} = 0$$

The boundary condition that raises the mechanical stress in the SEI layer is the interfacial velocity of the diffuse interface (correlate with the electrodeposition rate), described as

$$v = -\frac{kL_\eta}{\gamma} \left\{ \exp \frac{(1-\alpha)F\eta_a}{RT} - c_+ \exp \left[\frac{-\alpha F \eta_a - F \eta_m}{RT} \right] \right\}.$$

The simulation is implemented in COMSOL Multiphysics. The domain is 200 x 200 nm with the SEI layer. The perturbation in the middle represents the nucleation of dendrites (r = 4 nm). The overpotential of 0.1 V is applied to trigger the electrodeposition process. The velocity of the moving interface due to the electrodeposition process causes the movement of the SEI layer. The unequal growth rate along the surface results in the evolution of stress within the SEI layer. The pressure that develops at the interface locally feeds back to the growth rate of dendrites, influencing the overall electrodeposition behavior. In addition, as our focus is SEI mechanics, the ionic diffusion in the SEI is the same as that in the electrolyte. The phase-field parameters and the SEI properties are listed **Table S2** and **Table S3**, respectively.

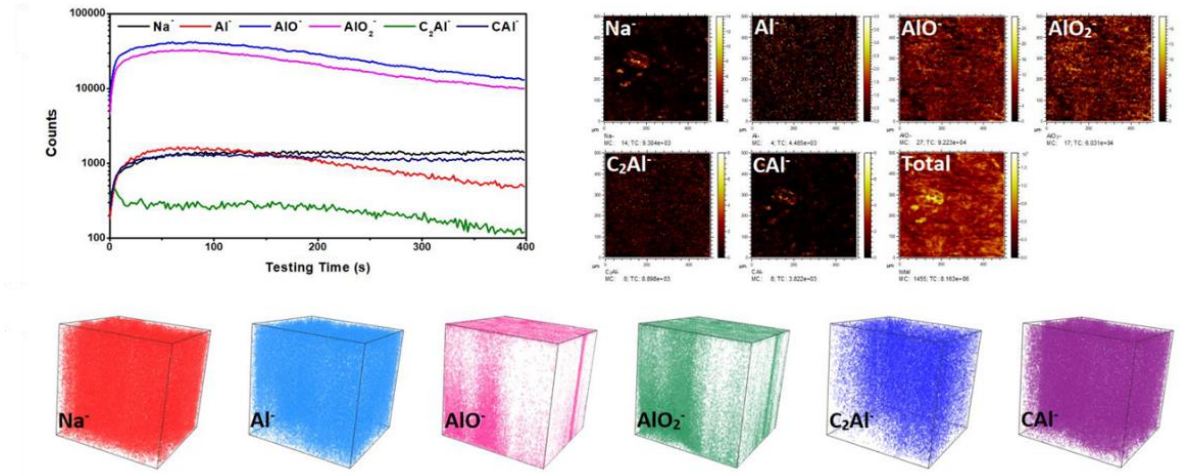

Figure S1 The TOF-SIMS secondary ion images, the depth profile of various secondary ion species and corresponding 3D images of Na@(2ALD-2MLD)4.

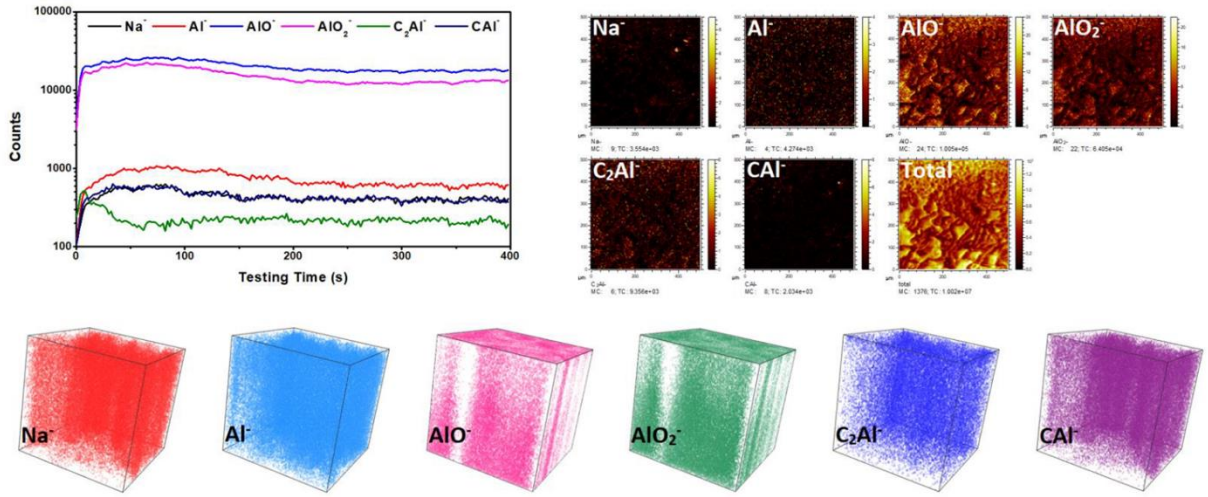

Figure S2 The TOF-SIMS secondary ion images, the depth profile of various secondary ion species and corresponding 3D images of Na@(5ALD-5MLD)2.

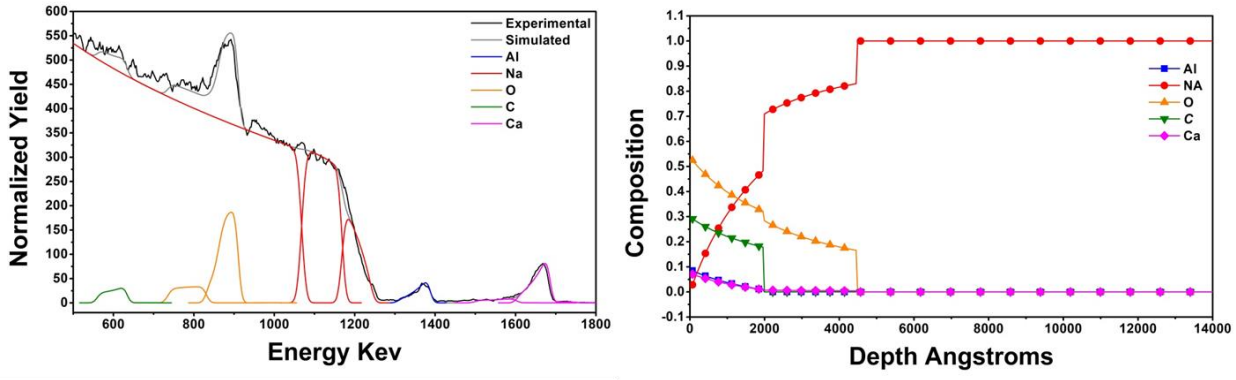

Figure S3 The RBS spectra and calculated depth profiles of Na@(2ALD-2MLD)4.

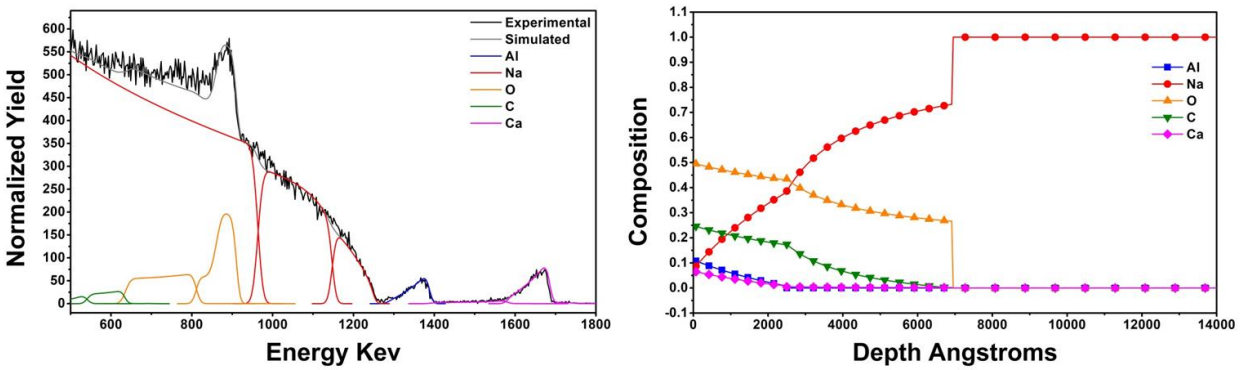

Figure S4 The RBS spectra and calculated depth profiles of Na@(5ALD-5MLD)2.

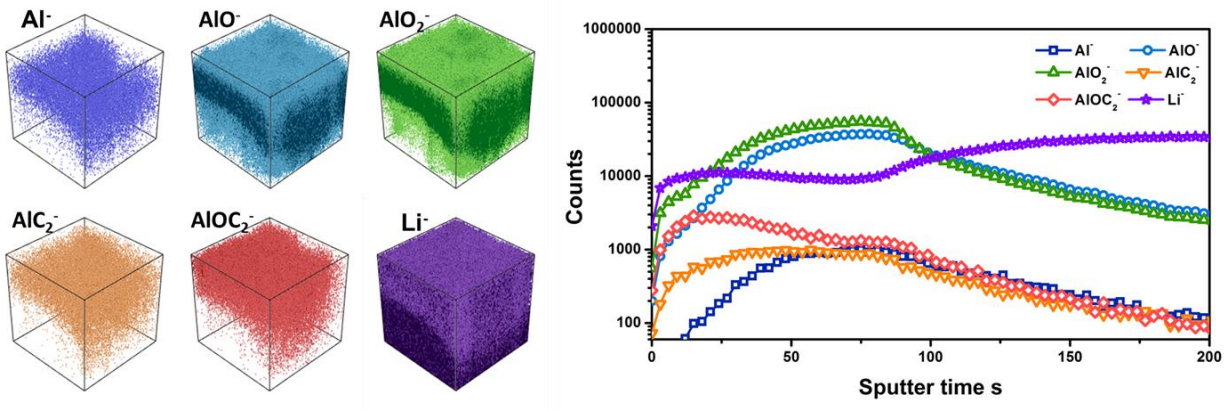

Figure S5 The TOF-SIMS secondary ion images, the depth profile of various secondary ion species and corresponding 3D images of Li@(1ALD-1MLD)10.

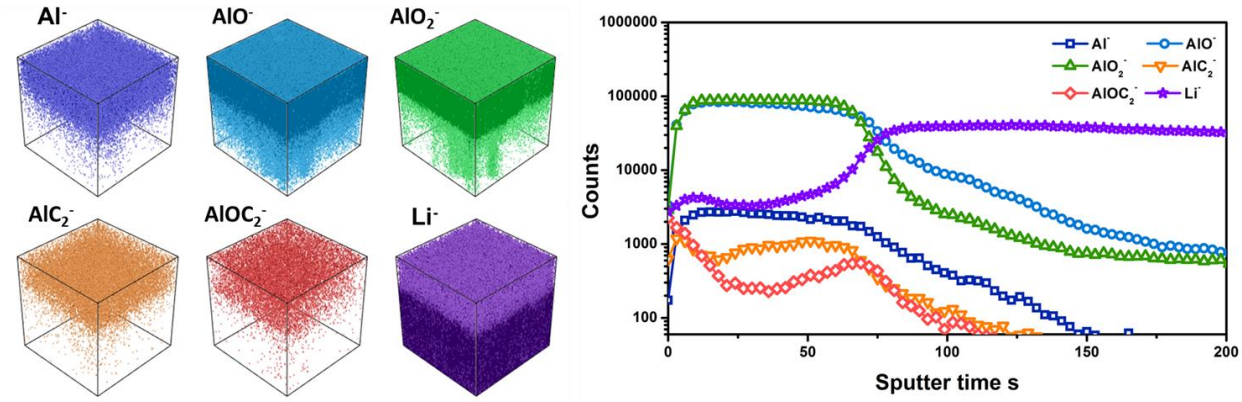

Figure S6 The TOF-SIMS secondary ion images, the depth profile of various secondary ion species and corresponding 3D images of Li@(1ALD-1MLD)25.

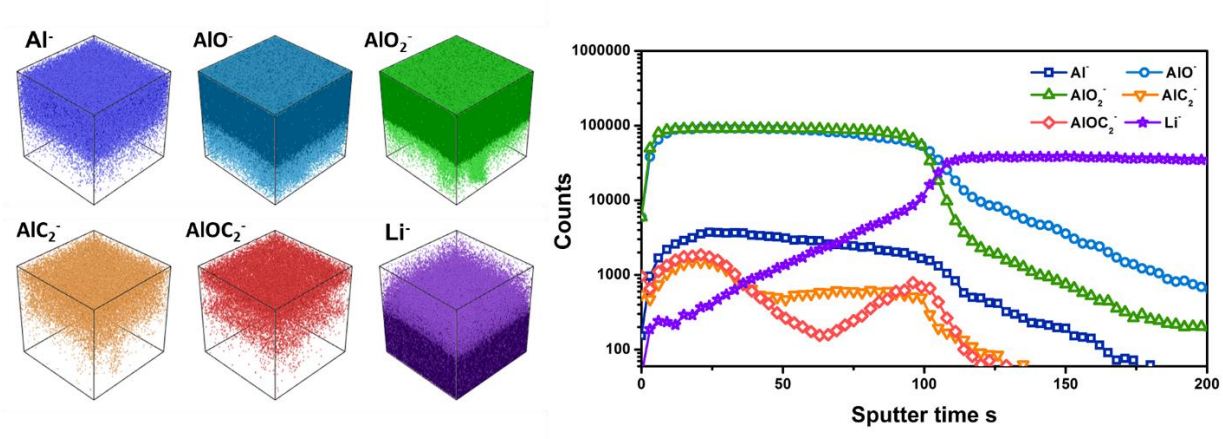

Figure S7 The TOF-SIMS secondary ion images, the depth profile of various secondary ion species and corresponding 3D images of Li@(1ALD-1MLD)50.

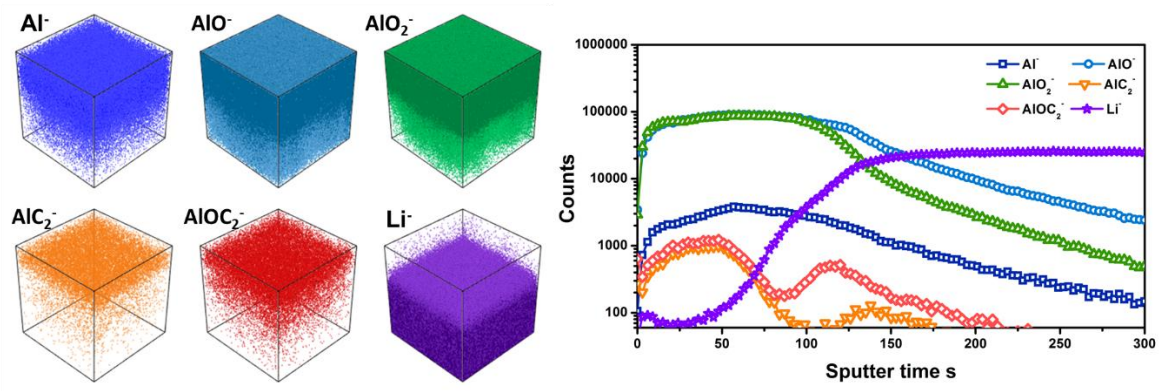

Figure S8 The TOF-SIMS secondary ion images, the depth profile of various secondary ion species and corresponding 3D images of Li@(2ALD-2MLD)25.

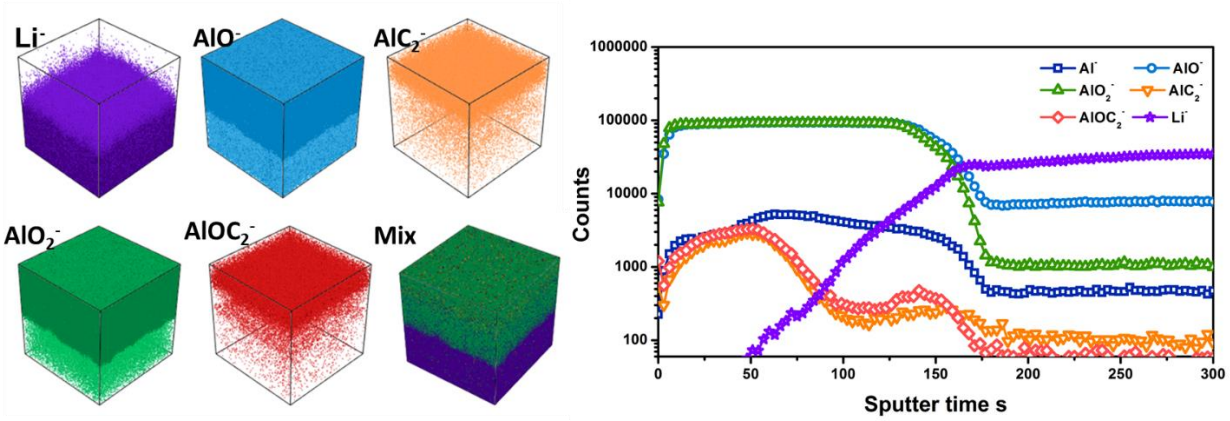

Figure S9 The TOF-SIMS secondary ion images, the depth profile of various secondary ion species and corresponding 3D images of Li@(5ALD-5MLD)10.

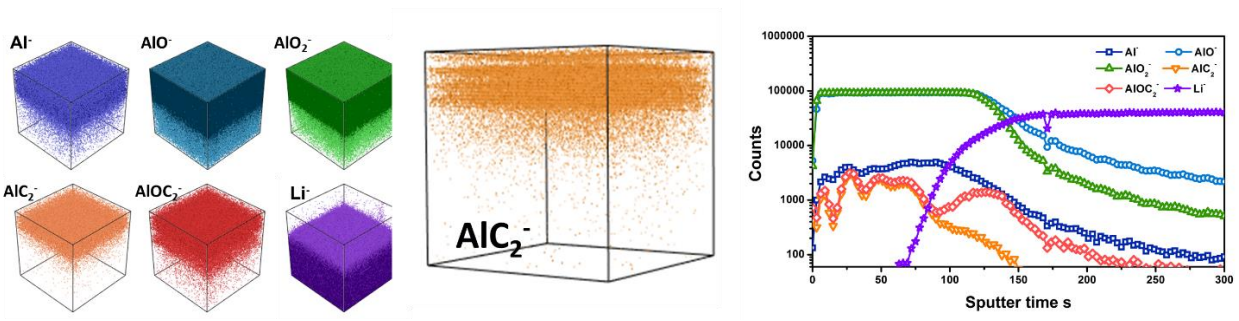

Figure S10 The TOF-SIMS secondary ion images, the depth profile of various secondary ion species and corresponding 3D images of Li@(10ALD-10MLD)5.

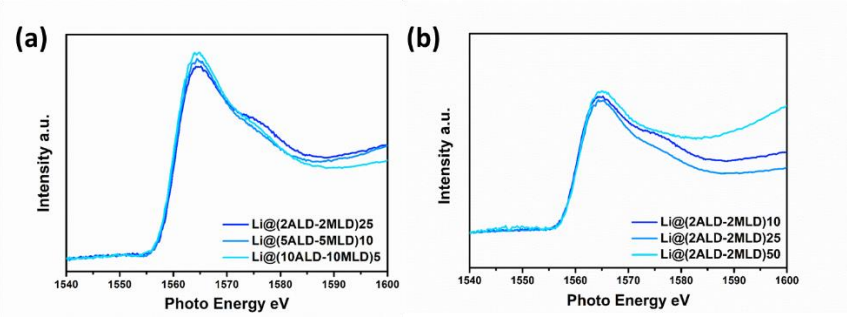

Figure S11 The XAS of Near-Edge Structure at Al K edge of (a) Li@(2ALD-2MLD)25, Li@(5ALD-5MLD)10 and Li@(10ALD-10MLD)5; (b) Li@(2ALD-2MLD)10, Li@(2ALD-2MLD)25, and Li@(2ALD-2MLD)50

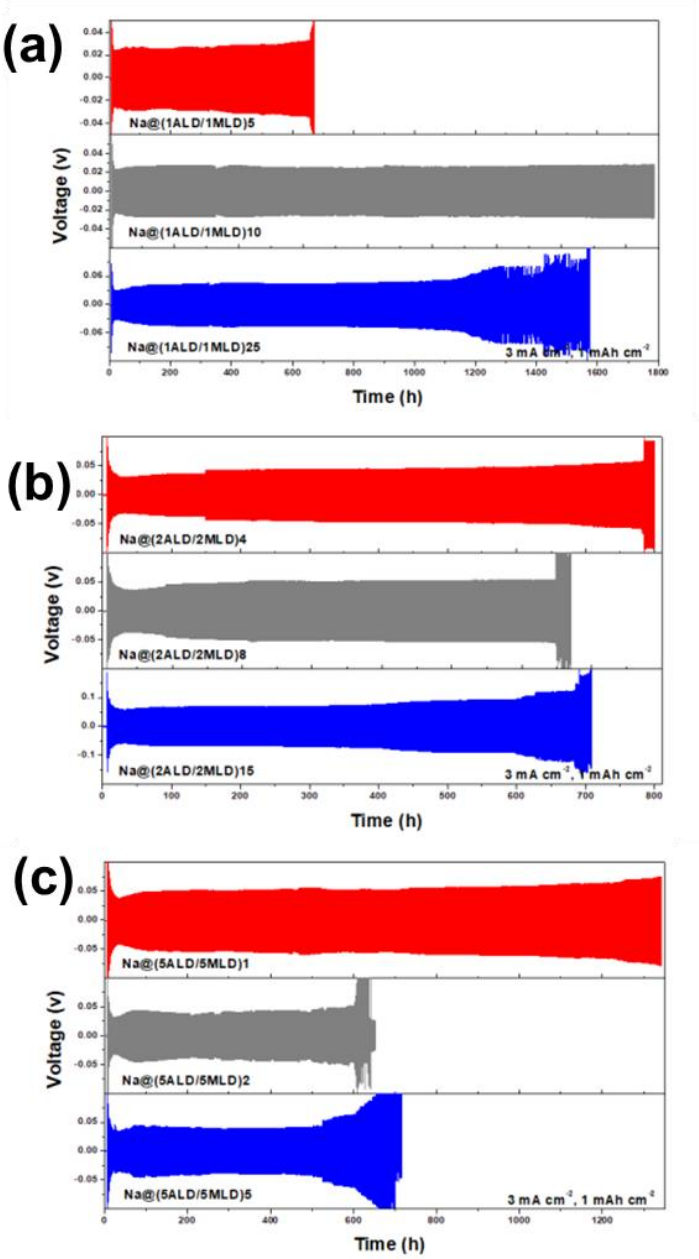

Figure S12 The electrochemical performances of Na/Na symmetric cells of (a) Na@(1ALD-1MLD)5, Na@(1ALD-1MLD)10 and Na@(1ALD-1MLD)25; (b) Na@(2ALD-2MLD)4, Na@(2ALD-2MLD)4 and Na@(2ALD-2MLD)15; (c) Na@(5ALD-5MLD)1, Na@(5ALD-5MLD)2 and Na@(5ALD-5MLD)5 at the current density of 3 mA cm^{-2} with the capacity limit of 1 mAh cm^{-2}.

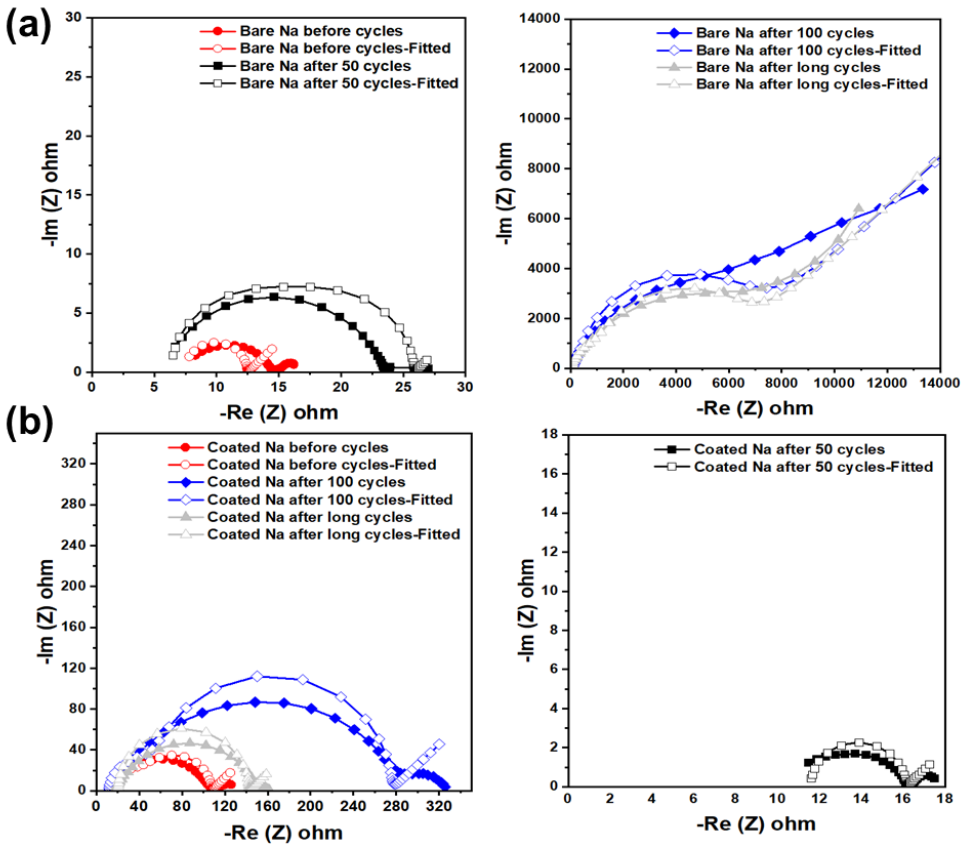

Figure S13 Nyquist plot showing electrochemical impedance spectroscopy (EIS) of (a) bare Na foil and (b) Na@(1ALD-1MLD)10 before and after cycling.

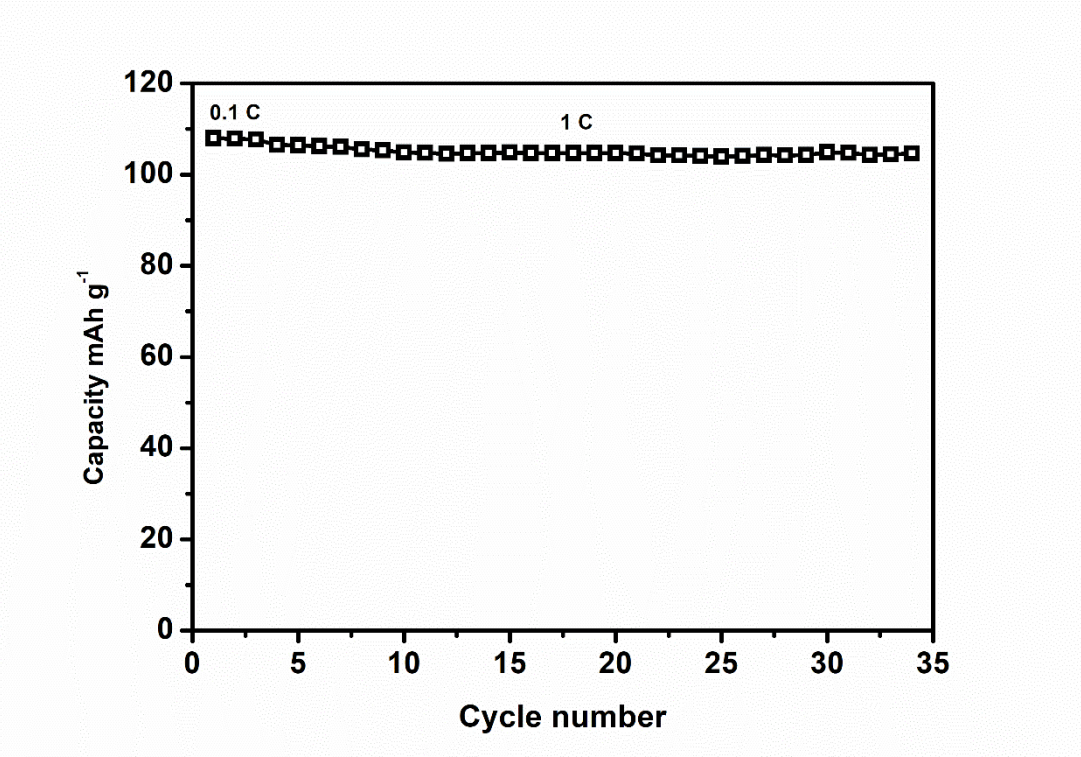

Figure S14 Cycling performances of full cell (Na- $Na_3V_2(PO_4)_3$)

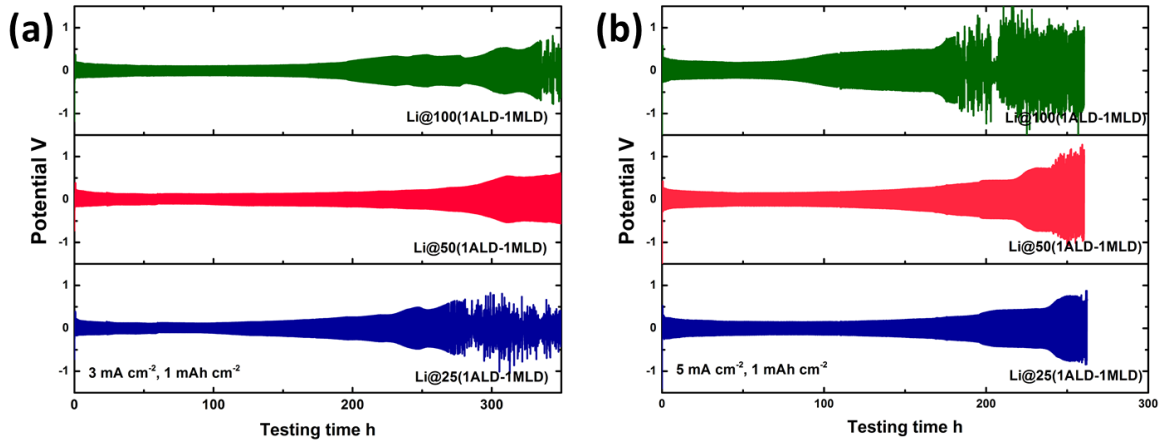

Figure S15 The electrochemical performances of Li/Li symmetric cells of Li@(1ALD-1MLD)25, Li@(1ALD-1MLD)50 and Li@(1ALD-1MLD)100 at the current density of (a) 3 mA cm^{-2} and (b) 5 mA cm^{-2} with the capacity limit of 1 mAh cm^{-2}.

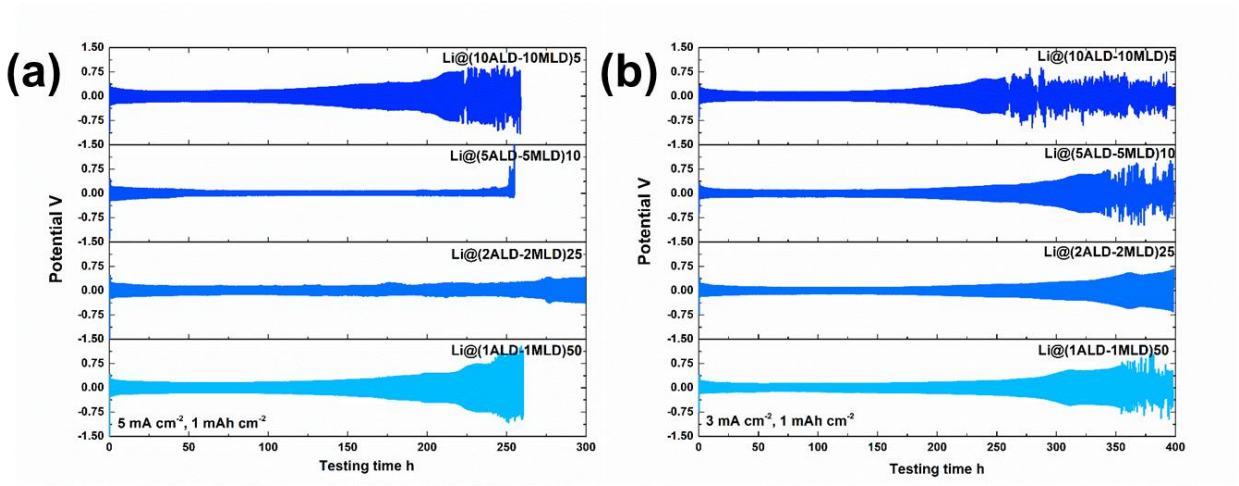

Figure S16 The electrochemical performances of Li/Li symmetric cells with different structures of Li@(1ALD-1MLD)50, Li@(2ALD-2MLD)25, Li@(5ALD-5MLD)10, and Li@(10ALD-10MLD)5 at the current density of (a) 5 mA cm^{-2} and (b) 3 mA cm^{-2} with the capacity limit of 1 mAh cm^{-2}.

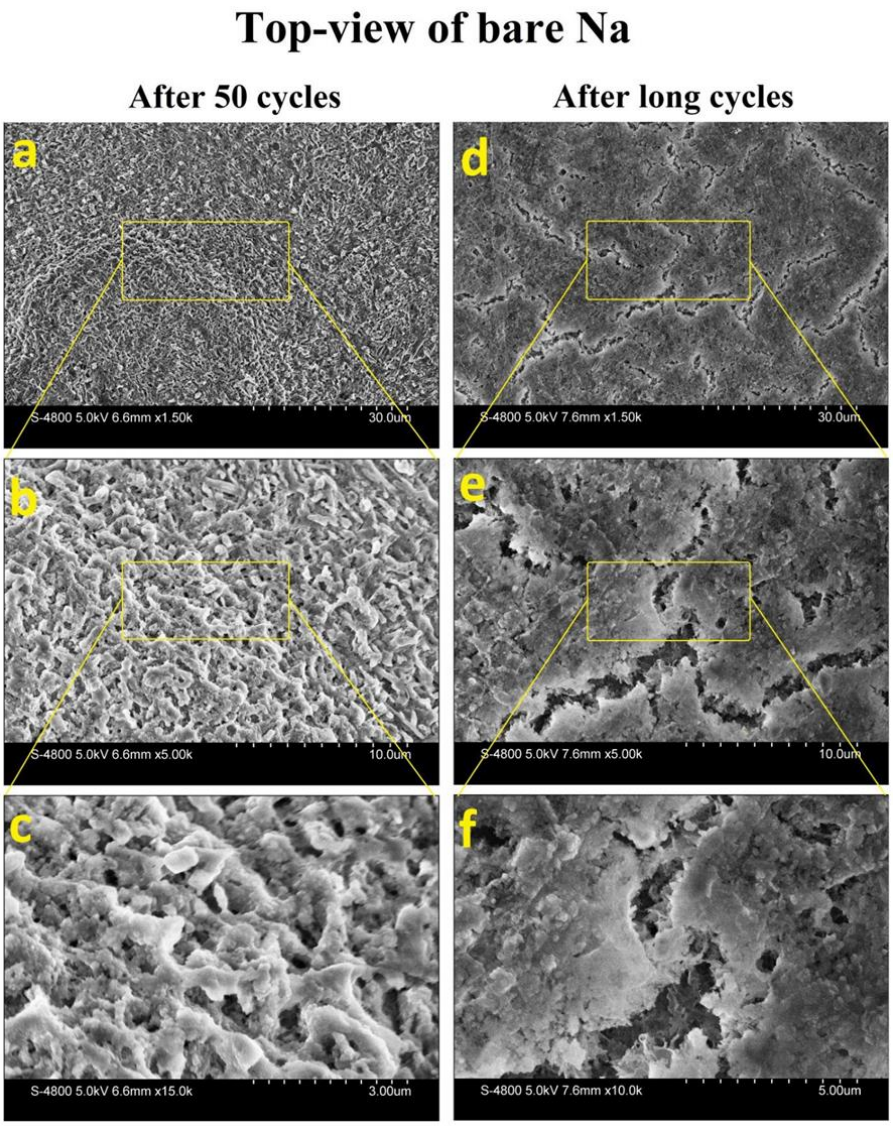

Figure S17 Top-view SEM images of bare Na foil after electrochemical cycling (50 cycles and long cycles).

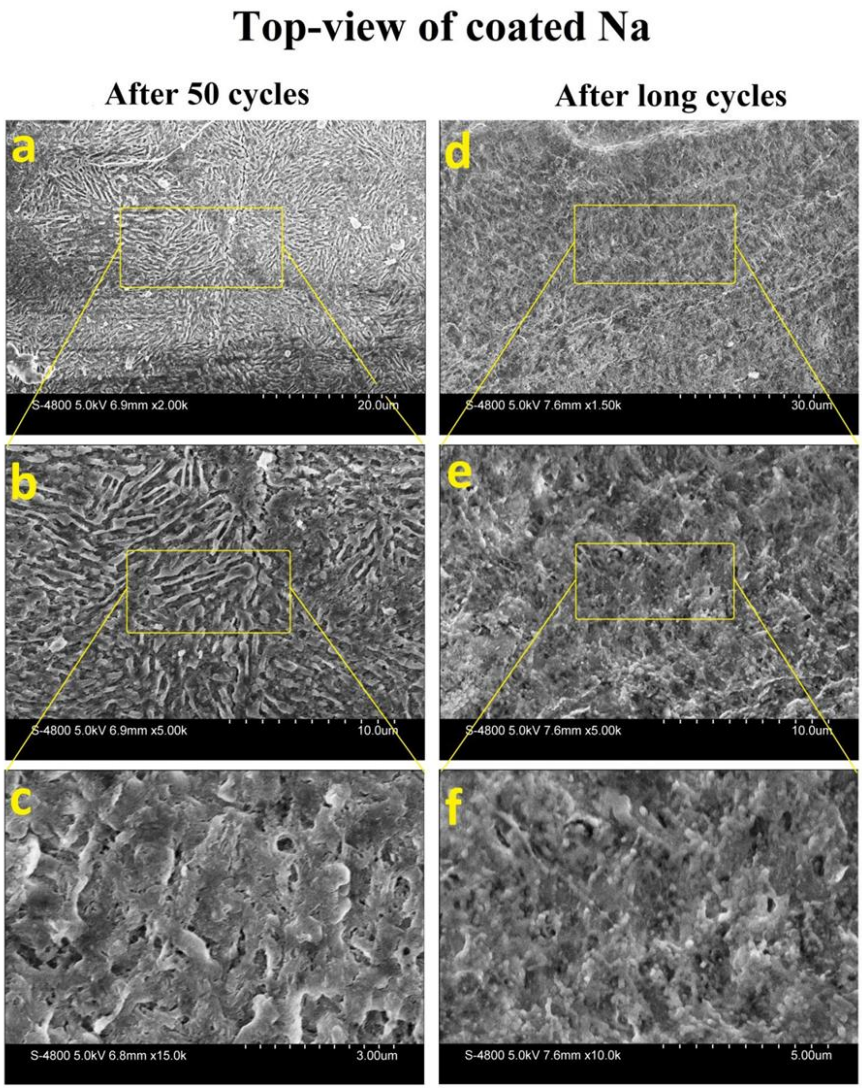

Figure S18 Top-view SEM images of Na@(1ALD-1MLD)10 after electrochemical cycling (50 cycles and long cycles).

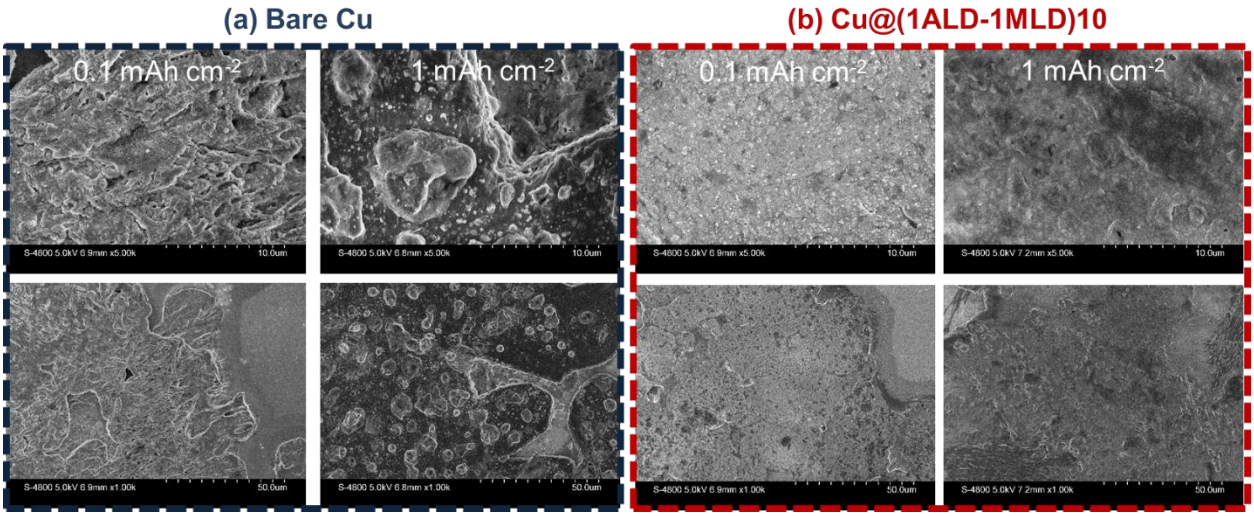

Figure S19 SEM images of Na deposition behavior on (a) Bare Cu foil and (b) Cu@(1ALD-1MLD)10 with different capacities of 0.1 mAh cm^{-2} and 1 mAh cm^{-2} at the current density of 1 mA cm^{-2}

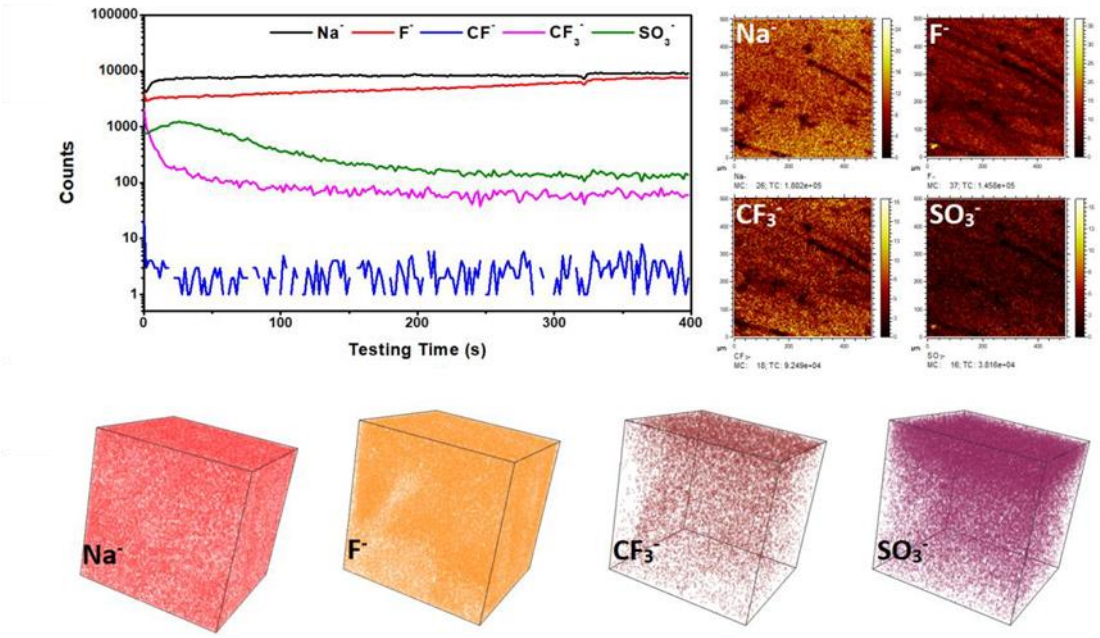

Figure S20 The TOF-SIMS depth profiles and corresponding 3D reconstructed images of bare Na foil after electrochemical cycling.

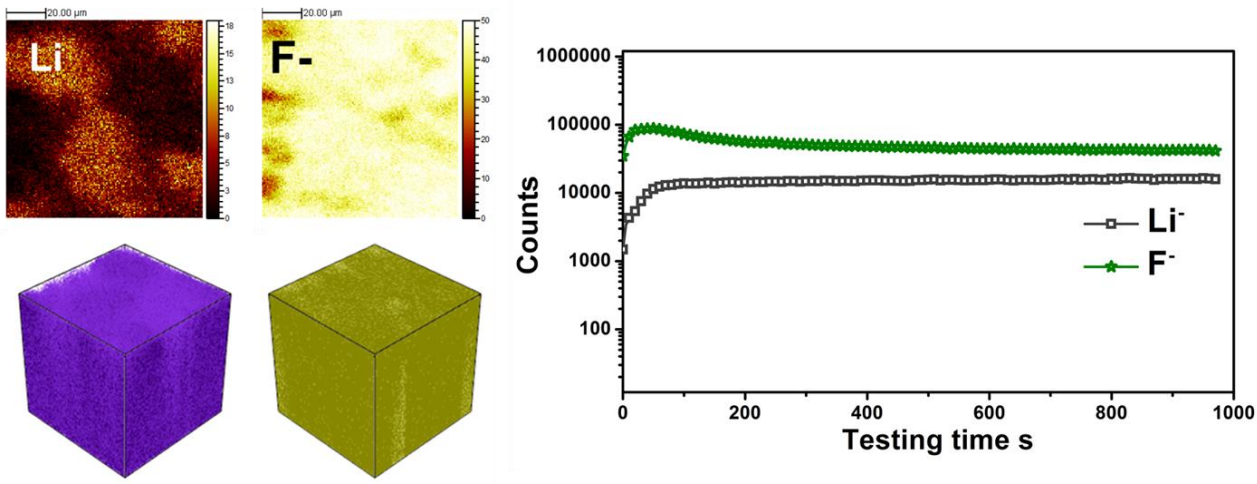

Figure S21 The TOF-SIMS depth profiles and corresponding 3D reconstructed images of bare Li foil after electrochemical cycling.

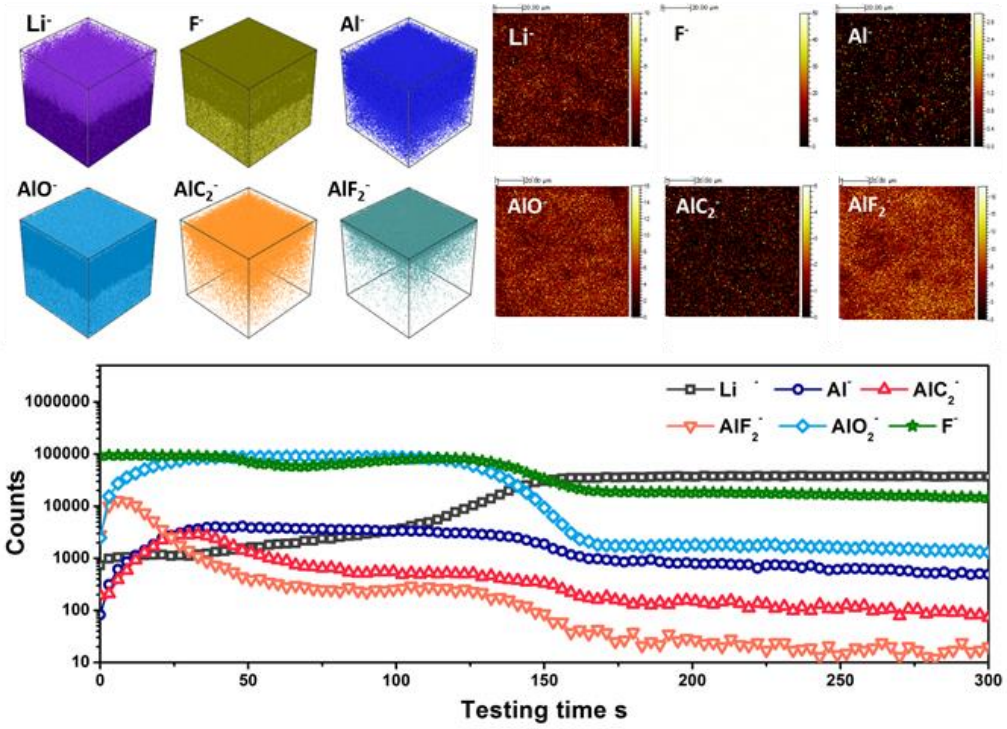

Figure S22 The TOF-SIMS depth profiles and corresponding 3D reconstructed images of Li@(1ALD-1MLD)50 after electrochemical cycling.

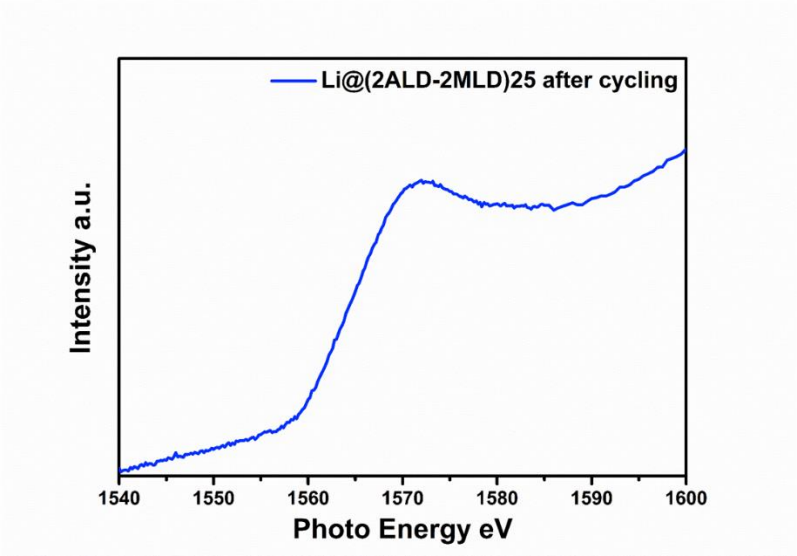

Figure S23 The XAS of Near-Edge Structure at Al K edge of Li@(2ALD-2MLD)25 after electrochemical cycling (10 cycles) in carbonate-based electrolyte at the current density of 1 mA cm^{-2} with the capacity limit of 1 mAh cm^{-2}.

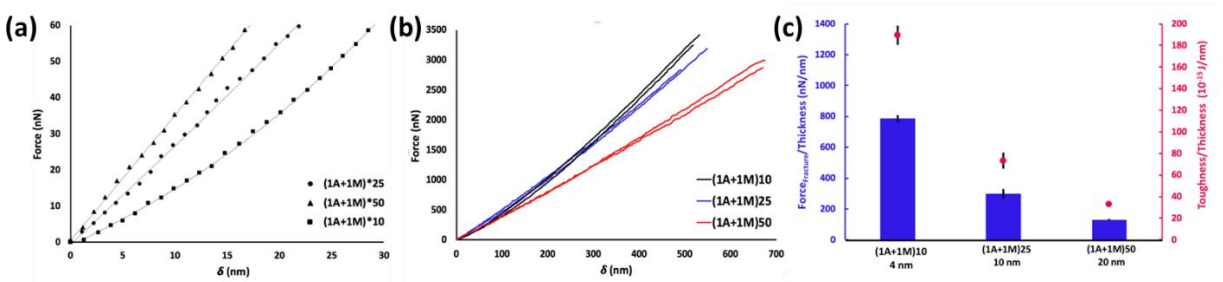

Figure S24 (a) Force-deflection (F-δ) curve of free-standing alloy films deflected in elastic regime, (b) Representative Force-deflection curve of the alloy films at failure, (c) The influence of film thickness on normalized failure force and normalized toughness for (1ALD-1MLD) alloy films.

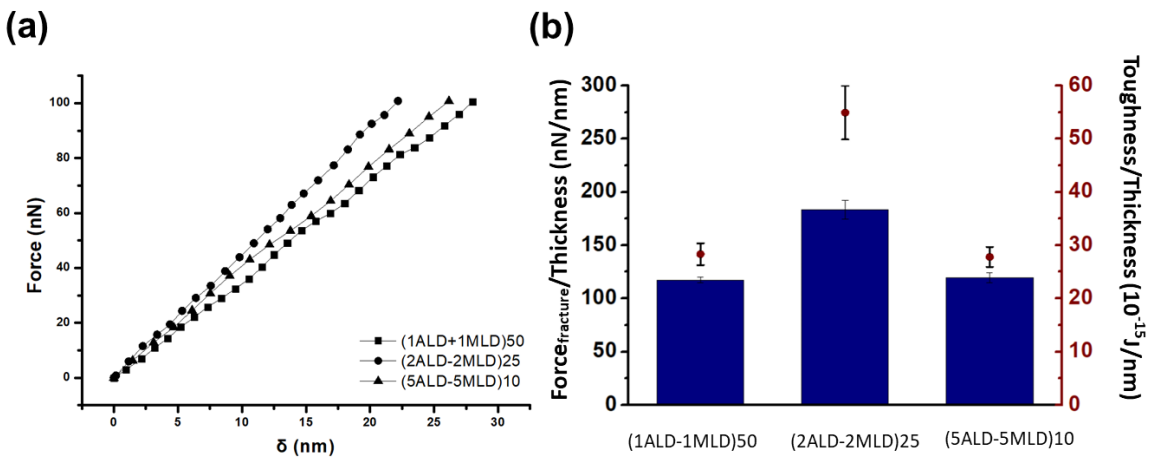

Figure S25 (a) Force-deflection (F-δ) curve of free-standing (1ALD-1MLD)50 alloy film and (5ALD-5MLD)10 nano-laminated film deflected in elastic regime, (b) The influence of film composition on failure force and toughness of alloy and nano-laminated films with 20 nm thickness.

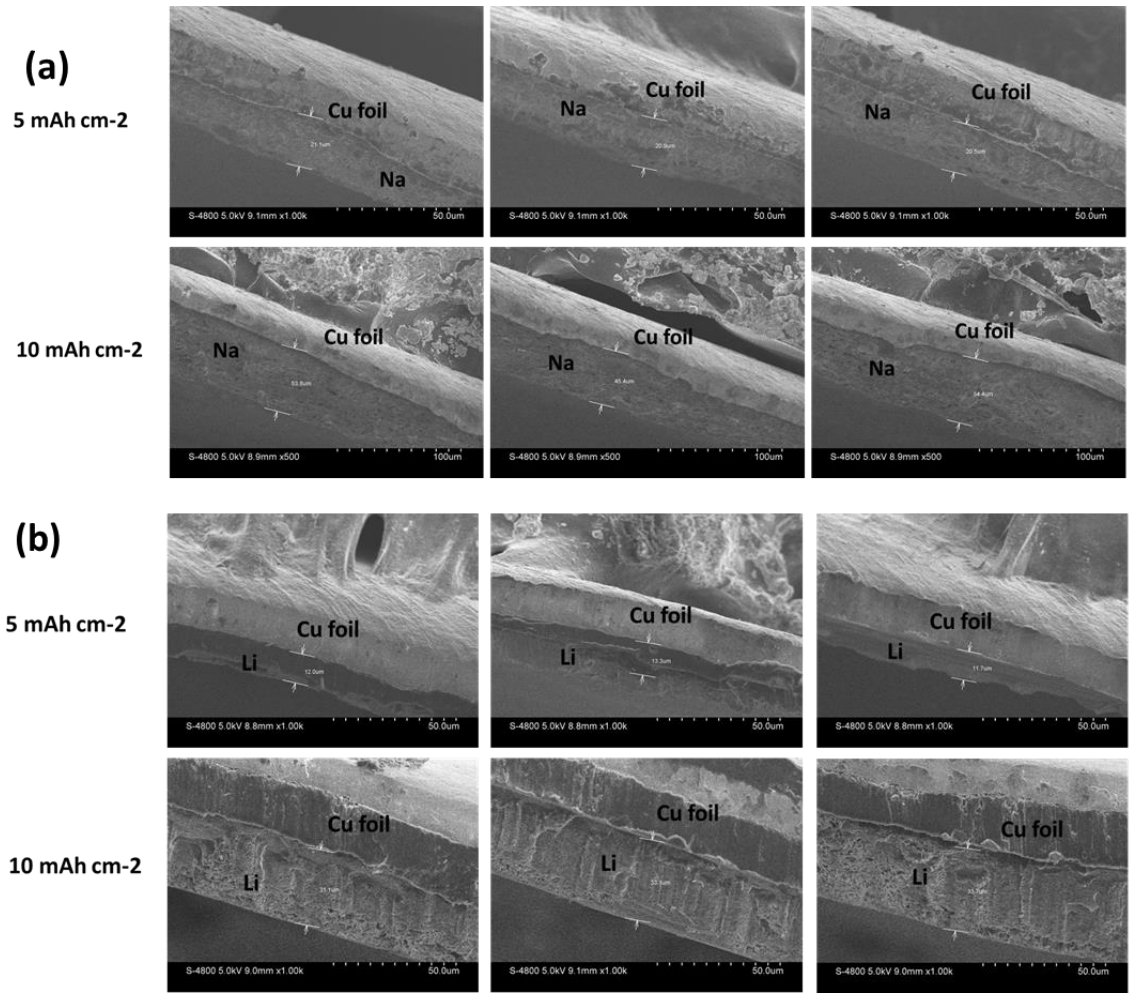

Figure S26 Cross sectional SEM images of deposited Na metal (a) and Li metal (b) on Cu foil at the current density of 3 mA cm^{-2} with different capacity.

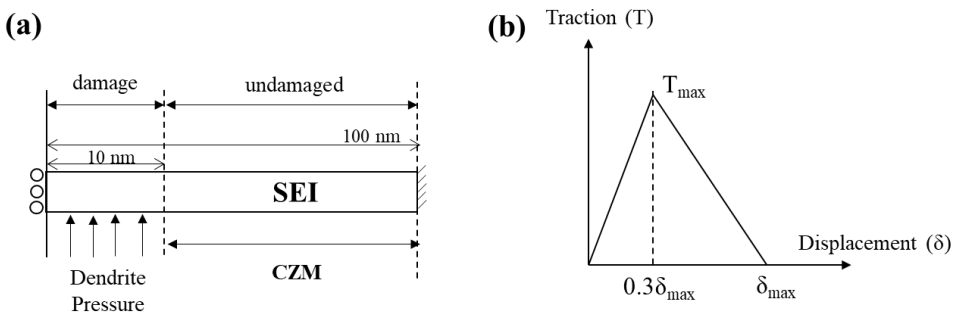

Figure S27 (a) Initial/boundary conditions of the mechanical delamination of the SEI. (b) A bilinear traction-separation governing the CZM.

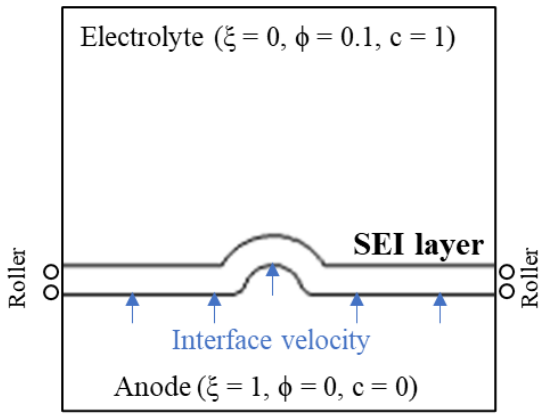

Figure S28 (a) Initial/boundary conditions of Phase-field Model for Dendrites with SEI Mechanics

Table S1 List of parameters and materials properties

Parameter	value	unit
Work of adhesion, W_{adh}	0.1	J m^{-2}
Max. displacement, δ_{max}	2	nm
Modulus, E_{SEI}	150	GPa
Poisson's ratio	0.3	1
SEI thickness	4-20	nm

Table S2 List of phase-field simulation parameters

Parameter	Value (unit)	Normalized value
Li-ion diffusion in electrolyte, D_e	0.8×10^{-9} (m^2/s)	30
Electrolyte conductivity, σ_e	1 (S/m)	10
Interfacial mobility, L_0	1×10^{3} ($m^3J^{-1}s^{-1}$)	24000
Reaction constant, L_η	1.3×10^{7} (s^{-1})	2000
Gradient energy Coeff. κ	4.8×10^{-9} (J/m)	0.008
Site dendrite of Li metal	7.64×10^{4} (mol/m^3)	-

Table S3 Properties of laminated SEI extracted from Figure S22a

	Thickness	E (GPa)
(1ALD+1MLD)10	4 nm	294
(1ALD+1MLD)25	10 nm	202
(1ALD+1MLD)50	20 nm	153